Tailor-Made Additives for Morphology Control in Molecular Bulk-Heterojunction Photovoltaics

Kenneth R. Graham,*[,†] Romain Stalder,[†] Patrick M. Wieruszewski,[†] Dinesh G. (Dan)Patel,[†] Danielle H. Salazar,[†] and John R. Reynolds*[,†,§]

[†]The George and Josephine Butler Polymer Research Laboratory, Department of Chemistry and Center for Macromolecular Science and Engineering, University of Florida, Gainesville, Florida 32611-7200, United States

[§]School of Chemistry and Biochemistry, School of Materials Science and Engineering, and Center for Organic Photonics and Electronics, Georgia Institute of Technology, Atlanta, Georgia 30332-0400, United States

S *Supporting Information*

ABSTRACT: Tailor-made additives, which are molecules that share the same molecular structure as a parent molecule with only slight structural variations, have previously been demonstrated as a useful means to control crystallization dynamics in solution. For example, tailor-made additives can be added to solutions of a crystallizing parent molecule to alter the crystal growth rate, size, and shape. We apply this strategy as a means to predictably control morphology in molecular bulk-heterojunction (BHJ) photovoltaic cells. Through the use of an asymmetric oligomer substituted with a bulky

triisobutylsilyl end group, the morphology of BHJ blends can be controlled resulting in a near doubling (from 1.3 to 2.2%) in power conversion efficiency. The use of tailor-made additives provides promising opportunities for controlling crystallization dynamics, and thereby film morphologies, for many organic electronic devices such as photovoltaics and field-effect transistors.

KEYWORDS: *morphology control, tailor-made additive, bulk-heterojunction, organic photovoltaic*
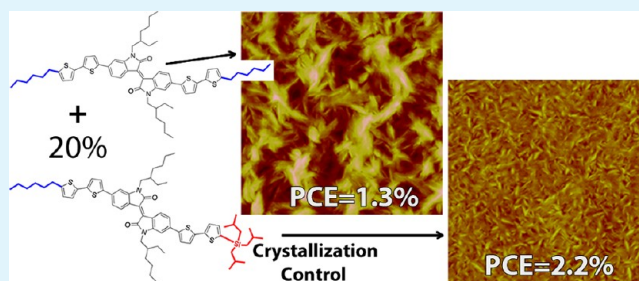
■ INTRODUCTION

Organic photovoltaics (OPVs) are quickly moving forward as potential alternatives to their more costly inorganic counterparts, in part due to the promise of low-cost fabrication via solution processing. Currently, power conversion efficiencies (PCEs) are approaching the 10% mark thought necessary for large-scale commercialization, with PCEs of 7−8%[1−4] for single junction polymer-based OPVs and 3−7%[5−9] for small molecule blends. Although solution processed small-molecule-based OPVs currently have lower PCEs than polymer-based OPVs, they present several advantages over polymeric cells including reproducible syntheses, no molecular weight variation, simpler purification, no end group contaminants, and easier functionalization. Small molecules can also be obtained with higher overall purities than polymers, which may lead to more stable devices as will be necessary for commercialization.

The efficiency of a bulk-heterojunction (BHJ) OPV cell is highly correlated with the morphology of the electron donor/electron acceptor blend film. Specifically, a BHJ OPV cell relies on an interconnected and interpenetrating network of domains rich in electron donor (D) and electron acceptor (A) materials, with dimensions on the order of the exciton diffusion length, typically 5−15 nm.[10−12] BHJ OPV devices also generally benefit from ordered or crystalline domains, which result in higher charge-carrier mobilities and thus improvements in the charge transport and charge extraction. Current methods

commonly employed to achieve this more desirable morphology include thermal annealing,[13,14] solvent annealing,[15,16] the use of solvent additives,[17,18] appropriate solvent selection,[19,20] and adjustment of processing parameters including spin speed and rate.[19] Although these methods all present promising ways to control morphology, the use of more reproducible and predictable techniques would be beneficial. These techniques for controlling morphology are particularly important as BHJ OPVs begin to transition from laboratory-scale processing techniques, such as spin coating, to commercial-scale printing techniques, such as slot-die coating,[21] screen printing,[22] or inkjet printing.[23]

The quest for more predictable control over morphologies has inspired the use of covalently linked D and A materials;[24] including fullerene containing copolymers,[25−29] polymers with fullerene end-groups,[30] and oligomers consisting of covalently linked D-A units.[31,32] The use of block copolymers as the sole material in the active layer of BHJ OPVs has resulted in decreased PCEs as compared to the noncovalently linked D-A blends;[24,25,27,29] however, these block copolymers have been found to have a beneficial effect on device stability when used as compatibilizers in D-A blends.[28,29] The use of covalently

linked D-A oligomers in single component BHJ OPVs has generally resulted in PCEs of less than 1.0%,[24] with the exception of a report by Bu et al. where clear morphology control was demonstrated resulting in a PCE of 1.5% with a maximum external quantum efficiency (EQE) of 46%.[32]

An alternative and attractive route with the potential to predictably tune the morphology of small molecule crystalline materials is the use of tailor-made additives. While there is only one such report involving the use of C_{60} as a tailor-made additive in BHJ OPVs,[33] they are well-established as a means of controlling crystallization rates in solution.[34−40] Tailor-made additives are structurally similar derivatives that are added to solutions of the crystallizing parent molecule to control the crystal nucleation and growth dynamics. For example, the addition of L-phenylalanine or L-leucine to a solution of L-alanine decreases the growth rate of L-alanine crystals.[37] Similarly, the addition of benzoic acid, o-toluamide, or p-toluamide to a solution of benzamide decreases crystal growth rates and alters the crystal shape.[34,35] In these examples, the structurally similar additive adsorbs onto a face of the growing crystal as illustrated in Figure 1, with the altered structure of the
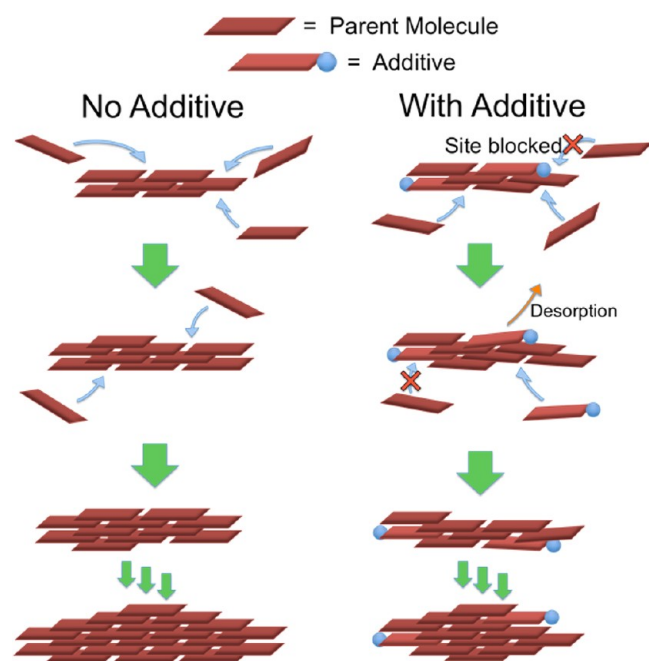

Figure 1. Schematic of the crystallization process in a solution containing a parent molecule and both a parent molecule and a monofunctionalized additive. The schematic demonstrates the reduction of crystal size due to adsorption and desorption of an additive onto the growing crystal.

additive hindering or preventing further molecules from being adsorbed. The additive generally remains there for some time before desorbing, thereby resulting in a net decrease of the crystal growth rate. Furthermore, if the additive selectively adsorbs onto a particular face (or faces) of the growing crystal, then the growth rate of that particular face (or faces) is decreased and the shape of the crystal is altered.[34−36] Alternatively, a nucleation inducing tailor-made additive may be added to the solution or film of the crystallizing parent molecule.[33,40,41] The introduction of this type of additive leads to more nucleation sites and thereby smaller crystal sizes.

The control of crystal sizes afforded by tailor-made additives presents an attractive method to precisely, predictably, and reproducibly tune the size of crystalline domains in polycrystalline films. For instance, growth-inhibiting additives may be used to reduce crystallite growth and hence provide a morphology consisting of smaller crystalline domains. Additionally, the size of these crystalline domains should, in principle, be readily tuned by simply adjusting the relative concentration of the tailor-made additive. With the control of crystal shape previously demonstrated, a tailor-made additive may also be designed to obtain a more desirable crystal shape for the particular application. For example, the tailor-made additive may be designed such that it leads to the formation of thinner and more needle-like crystals as may be desirable for OPV or organic field-effect transistor (OFET) applications. It is also known that charge-carrier mobilities may vary by orders of magnitude depending on the crystallographic direction.[42] Given this mobility dependence and the control of crystal growth afforded by tailor-made additives, it can be envisioned that the morphology of crystalline materials may be tuned to create needle-like crystals with the long axis corresponding with the direction of highest charge-carrier mobility.

The necessity of methods for reproducible and facile morphology control in organic photovoltaics, along with the unprecedented control of crystallization dynamics afforded by tailor-made additives, inspired the application of tailor-made additives to control morphology in BHJ OPV films. In this work, two tailor-made additives, which are structurally similar to the electron donating isoindigo-based oligomer previously reported with the addition of one or two bulky end groups,[43] are applied to reduce the crystallization rate of the parent oligomer and thereby control film morphologies in oligomer/fullerene blends. The effects of the tailor-made additives on crystallization dynamics are probed through measuring the size of crystals formed in solution through cross-polarized optical microscopy and probing the crystallization behavior with differential scanning calorimetry (DSC) and UV-vis absorbance spectroscopy. The effects of the tailor-made additives on the morphology of oligomer/fullerene blend films are explored with atomic force microscopy (AFM) and transmission electron microscopy (TEM), with these morphologies being correlated with hole mobilities as measured in space-charge limited current devices and the performance of OPV cells. Both additives are shown to decrease domain sizes in oligomer/fullerene blend films, with the singly substituted additive leading to improved OPV performance.

■ EXPERIMENTAL SECTION

Synthetic Details. Commercially available reagents were used as received from the chemical suppliers. Reactions that required anhydrous conditions were carried out under an inert atmosphere of argon in flame-dried glassware. Toluene and tetrahydrofuran were dried using a Solvent Purification System and degassed by three freeze−pump−thaw cycles. ^{1}H-NMR and ^{13}C-NMR spectra were collected on a Varian Inova 2 500 MHz instrument using $CDCl_3$ as a solvent and the residual $CHCl_3$ peak as references (^{1}H: δ = 7.26 ppm; ^{13}C: δ = 77.23 ppm). Mass spectra were recorded on either a Finnigan MAT95Q Hybrid Sector (EI, HRMS) or a Bruker Reflex II (MALDI-TOF) mass spectrometer operated in linear mode with delayed extraction. Elemental analyses were carried out by the CHN elemental analysis service in the Chemistry Department of the University of Florida. 2-(5-Hexylthiophen-2-yl)-4,4,5,5-tetramethyl-1,3,2-dioxaborolane was purchased from Sigma-Aldrich and used without further

purification. The synthesis of 6,6′-dibromo-N,N′-di(2-ethylhexyl)-isoindigo (1) was reported elsewhere.[43]

(5′-Bromo-[2,2′-bithiophen]-5-yl)triisobutylsilane (2). 5,5′-Dibromo-2,2′-bithiophene (3.24 mg, 10 mmol) was loaded in a 250 mL dry flask under an argon flow and dissolved in anhydrous tetrahydrofuran (100 mL). The solution was stirred and cooled to −78 °C, after which a solution of *n*-butyllithium (7.1 mL, 10 mmol) was added dropwise to the reaction mixture over the course of 30 minutes. The solution was then stirred at −78 °C for 2 h, and then chlorotriisobutylsilane (2.58 g, 11 mmol) was added using a syringe via a septum, in one portion. The mixture was allowed to warm up to room temperature while stirring for 12 h. The solution was then concentrated and rediluted with hexanes (100 mL). The afforded white precipitate was filtered off, and the remaining clear solution was concentrated to a brown slurry. This was purified by column chromatography on silica using pure hexanes as eluent, to afford the title compound (1.51 g, 3.5 mmol, 35 %) as a clear oil. ^{1}H NMR (CDCl$_3$): δ 7.15 (d, J = 3.5 Hz, 1H), 7.12 (d, J = 3.5 Hz, 1H), 6.96 (d, J = 3.8 Hz, 1H), 6.93 (d, J = 3.8 Hz, 1H), 1.83 (nonuplet, J = 6.6 Hz, 3H), 0.92 (d, J = 6.6 Hz, 18H), 0.86 (d, J = 6.9 Hz, 6H). ^{13}C NMR (CDCl$_3$): δ 141.44, 139.32, 139.28, 135.59, 130.78, 125.22, 123.85, 110.94, 26.69, 25.38, 25.07.

Triisobutyl(5′-(4,4,5,5-tetramethyl-1,3,2-dioxaborolan-2-yl)-[2,2′-bithiophen]-5-yl)silane (3). Compound 2 (650 mg, 1.47 mmol) was dissolved in a dry flask with anhydrous tetrahydrofuran (10 mL) and cooled to −78 °C. A solution of *n*-butyllithium in hexanes (1.25 mL, 1.75 mmol) was added dropwise to the reaction mixture, and the solution was then stirred at −78°C for 2 h. 2-Isopropoxy-4,4,5,5-tetramethyl-1,3,2-dioxaborolane (355 mg, 1.91 mmol) was added using a syringe via a septum, in one portion. The mixture was allowed to warm up to room temperature while stirring for 12 h. The mixture was then diluted with hexanes, poured in water, and extracted twice with hexanes. After washing the combined organic extracts with brine, the solution was dried over magnesium sulfate. The volatiles were then evaporated to afford a yellow oil. The crude oil contained 70 % of the title compound, the remaining being unreacted starting material as determined by ^{1}H NMR. This was used without further purification. ^{1}H NMR (CDCl$_3$): δ 7.51 (d, J = 3.6 Hz, 1H), 7.27 (d, J = 3.8 Hz, 1H), 7.19 (d, J = 4.3 Hz, 1H), 7.14 (d, J = 4.8 Hz, 1H), 1.83 (nonuplet, J = 6.6 Hz, 3H), 1.35 (s, 12H), 0.92 (d, J = 6.6 Hz, 18H), 0.86 (d, J = 6.9 Hz, 6H).

(E)-1,1′-bis(2-Ethylhexyl)-6,6′-bis(5′-hexyl-[2,2′-bithiophen]-5-yl)-[3,3′-biindolinylidene]-2,2′-dione (1-C6₂) and (E)-1,1′-bis(2-Ethyl-hexyl)-6-(5′-hexyl-[2,2′-bithiophen]-5-yl)-6′-(5′-(triisobutylsilyl)-[2,2′-bithiophen]-5-yl)-[3,3′-biindolinylidene]-2,2′-dione (2-C6Si). In a Schlenk flask under argon atmosphere, 6,6′-dibromo-N,N′-di(2-ethylhexyl)isoindigo (1, 291 mg, 0.45 mmol), 2-(5-hexylthiophen-2-yl)-4,4,5,5-tetramethyl-1,3,2-dioxaborolane (296 mg, 0.79 mmol), Pd$_2$(dba)$_3$ (30 mg, chloroform adduct), and P(*o*-tolyl)$_3$ (20 mg) were loaded under a flux of argon and then kept under vacuum for 30 min, during which the flask was subjected to three vacuum-argon purge cycles, and finally refilled with argon. Degassed toluene (4 mL) was then added to the flask, followed by a degassed aqueous solution of tetraethylammonium hydroxide (1.8 mL, 1.8 mmol). The mixture was stirred and heated up to 90 °C. The progess of the reaction was monitored by thin-layer chromatography (TLC), using a 3:2 mixture of hexanes/dichloromethane as eluent. When complete consumption of the dibromoisoindigo (red spot, Rf = 0.5) starting material was confirmed by TLC, a solution of compound 3 (166 mg, 0.34 mmol) in degassed toluene (2 mL) was added to the flask. The mixture was kept stirring at 90 °C for 12 h, then allowed to cool to room temperature, and slowly precipitated in methanol (40 mL). The precipitates were filtered and collected in a 100 mL round-bottom flask, to which a minimum amount of hot chloroform (~15 mL) was added in order to dissolve the solids completely. Silica gel (15 mL) was then added to the flask and swirled. Careful evaporation of the solvent adsorbed the crude onto the dry silica gel, which was loaded onto a silica gel column packed with 2:1 hexanes/dichloromethane. Eluting with 2:1 and then 3:2 hexanes/dichloromethane separated and purified the two title compounds, affording 1-C6₂ (178 mg, 0.18 mmol, 40%) and 2-C6Si (144 mg, 0.13 mmol, 29%) as dark purple−blue solids.

1-C6₂, ^{1}H-NMR (CDCl$_3$): δ 9.01 (d, J = 8.7, 2H), 7.25−7.18 (m, 4H), 7.05 (d, J = 3.6 Hz, 2H) 7.02 (d, J = 3.6 Hz, 2H), 6.78 (s, 2H), 6.70 (d, J = 3.3 Hz), 3.68−3.41 (m, 4H), 2.80 (t, J = 4.2 Hz, 4H), 1.82−1.65 (m, 6H), 1.44−1.20 (m, 28H), 0.98−0.81 (m, 18H). ^{13}C-NMR (CDCl$_3$): δ 168.73, 146.34, 145.61, 142.10, 138.90, 137.43, 134.72, 131.68, 130.34, 125.12, 125.07, 124.19, 123.90, 121.18, 118.80, 104.53, 44.24, 38.05, 31.79, 31.75, 31.12, 30.41, 29.26, 29.03, 24.54, 23.35, 22.81, 14.45, 14.36, 11.03. HRMS (ESI-TOF) Calculated for C$_{60}$H$_{74}$N$_2$O$_2$S$_4$ (M + H)$^+$: 983.4706. Found: m/z 983.4741. Anal. Calcd. for C$_{60}$H$_{74}$N$_2$O$_2$S$_4$: C, 73.27; H, 7.58; N, 2.85. Found: C, 73.39; H,7.57; N, 2.80.

2-C6Si ^{1}H-NMR (CDCl$_3$): δ 9.10 (dd, J = 3.0, 1.8 Hz, 1H), 9.08 (dd, J = 3.0, 1.8 Hz, 1H), 7.29 (d, J = 3.8 Hz, 1H), 7.28 (d, J = 3.5 Hz, 1H), 7.27 (d, J = 3.8 Hz, 1H), 7.25 (dd, J = 4.2, 1.6 Hz, 1H), 7.23 (dd, J = 4.0, 1.6 Hz, 1H), 7.17 (d, J = 3.8 Hz, 1H), 7.16 (d, J = 3.4 Hz, 1H), 3.71−3.53 (m, 4H), 2.80 (t, J = 7.4 Hz, 2H), 1.86 (nonuplet, J = 6.6 Hz, 3H), 1.86−1.76 (br, 2H), 1.70 (quintet, J = 7.2 Hz, 2H), 1.43−1.28 (m, 24H), 0.95 (d, 6.6 Hz, 18H), 0.88 (d, J = 6.8 Hz, 6H), 0.96−0.87 (m, 15H). ^{13}C-NMR (CDCl$_3$): δ 168.81, 146.34, 145.79, 145.77, 142.73, 142.16, 142.14, 139.52, 138.97, 138.48, 137.56, 137.47, 135.78, 134.71, 131.87, 131.75, 130.38, 130.37, 125.35, 125.23, 125.20, 125.18, 124.96, 124.22, 123.99, 121.30, 121.19, 118.97, 118.91, 104.69, 104.65, 44.27, 38.03, 31.83, 31.08, 30.48, 29.21, 29.18, 29.03, 26.75, 26.70, 25.44, 25.13, 24.56, 23.35, 22.83, 14.42, 14.34, 11.07. Anal. Calcd for C$_{66}$H$_{88}$N$_2$O$_2$S$_4$Si: C, 72.21; H, 8.08; N, 2.55. Found: C, 72.51; H, 8.56; N, 2.48

(E)-1,1′-bis(2-Ethylhexyl)-6,6′-bis(5′-(triisobutylsilyl)-[2,2′-bithio-phen]-5-yl)-[3,3′-biindolinylidene]-2,2′-dione (3-Si₂). In a purged Schlenk flask, 6,6′-dibromo-N,N′-di(2-ethylhexyl)isoindigo (1, 220 mg, 0.34 mmol), compound 3 (470 mg, 0.89 mmol), Pd$_2$(dba)$_3$ (15 mg, chloroform adduct), and P(*o*-tolyl)$_3$ (10 mg) were loaded under a flux of argon and then kept under vacuum for 30 min, during which the flask was subjected to three vacuum-argon purge cycles, and finally refilled with argon. Degassed toluene (5 mL) was then added to the flask, followed by a degassed aqueous solution of tetraethylammonium hydroxide (1.4 mL, 1.4 mmol). The mixture was stirred and heated to 90°C for 12 h. After cooling back to room temperature, the mixture was slowly poured in methanol (30 mL) and the precipitates were collected by filtration. The solids had enough solubility that they were dissolved in a minimum volume of 3:2 hexanes/dichloromethane and purified by column chromatography using 3:2 hexanes/dichloro-methane as eluent. This afforded the title compound (265 mg, 0.22 mmol, 64%) as a dark gray-purple solid. ^{1}H NMR (CDCl$_3$): δ 9.13 (dd, J = 4.2, 1.6 Hz, 1H), 7.32 (d, J = 3.8 Hz, 1H), 7.29 (d, J = 3.5 Hz, 1H), 7.27 (dd, J = 4.2, 1.7 Hz, 1H), 7.20 (d, J = 3.8 Hz, 1H), 7.17 (d, J = 3.5 Hz, 1H), 6.92 (t, J = 1.7 Hz, 1H), 3.76−3.60 (m, 2H), 1.86 (nonuplet, 6.6 Hz, 4H), 1.46−1.30 (m, 8H), 1.00−0.90 (m, 30H). ^{13}C NMR (CDCl$_3$): δ 168.86, 145.88, 142.71, 142.14, 139.55, 138.53, 137.60, 135.75, 131.92, 130.37, 125.34, 125.27, 124.95, 121.29, 119.06, 104.77, 38.01, 31.05, 29.16, 26.71, 25.41, 25.09, 24.51, 23.33, 14.38, 11.04. Anal. Calcd for C$_{72}$H$_{102}$N$_2$O$_2$S$_4$Si$_2$: C, 71.35; H, 8.48; N, 2.31. Found: C, 71.62; H, 9.04; N, 2.23.

Solution Crystallization. Separate solutions of the symmetric and asymmetric oligomers in chlorobenzene were prepared at 1.0 mg/mL. These solutions were then combined to form solutions of the appropriate ratios of the two oligomers. A known volume of these solutions was added to known volumes of hexanes to form solutions with a total concentration of 0.05 mg/mL. These solutions were all heated on a hot plate at 60 °C, at which temperature the oligomer appeared fully dissolved. The solutions were then left to cool to room temperature over 3 h. After the solutions were cooled, they were drop cast on cleaned glass microscope slides or freshly cleaved mica pieces for analysis with the optical microscope or atomic force microscope (AFM), respectively. The optical microscope images were taken with and without cross-polarizers. The crystal lengths were measured from the optical microscope images with reported lengths representing the average length of 50 to 100 crystals, with error bars given as ± the standard error.

Photovoltaic Device Preparation. Indium tin oxide (ITO) coated glass substrates (15 Ω/square) were cleaned by briefly and

65

dx.doi.org/10.1021/am301944g | ACS Appl. Mater. Interfaces 2013, 5, 63−71

lightly scrubbing the surface with a sodium dodecyl sulfate solution soaked Kimwipe for ca. 10 s, followed by sequential sonication in a sodium dodecyl sulfate solution, deionized water (18 MΩ), acetone, and isopropanol for 15 min each. The substrates were blown dry with filtered nitrogen, exposed to an oxygen plasma for 20 min, and spin coated with poly(3,4-ethylenedioxythiophene)/polystyrene sulfonate (PEDOT:PSS) (Clevios P VP Al 4083) at 5000 rpm for 40 s. The coated substrates were transferred into an argon atmosphere glovebox (generally <0.1 ppm O_2 and H_2O) and annealed for 20 min at 130 °C. Individual solutions of the active materials were prepared in the glovebox at 20 mg/mL in chlorobenzene, stirred overnight at ambient temperature, and heated to 60 °C for 1−2 h to ensure dissolution. The solutions were then combined to give the appropriate weight ratios, stirred another 1−2 h at 60 °C, filtered through glass syringes fitted with 0.45 μm polytetrafluoroethylene (PTFE) filters, and spin coated onto the PEDOT:PSS coated substrates at 1000 rpm for 60 s. Films were annealed in the glovebox at 100 °C for 20 min before being transferred to a thermal vapor deposition chamber, where they remained under vacuum for 4−5 h prior to deposition of 10 nm of Ca and 100 nm of Al at a pressure of 1×10^{-6} mbar through shadow masks defining 8 independent pixels with 3 mm diameter (0.071 cm^2 area). The current−voltage characteristics of the devices were measured under 100 mW/cm^2 illumination from a Xe arc lamp fitted with an AM1.5G filter. All values are the average of a minimum of 6−8 cells, and the error is reported as ±1 standard deviation.

Morphology Characterization. Films were prepared as detailed above for morphology characterization. Tapping mode AFM images were recorded within 1−2 mm of the active region of the solar cells with a Veeco Innova scanning probe microscope (SPM) equipped with MikroMasch NSC15 tips with a resonant frequency of ~325 kHz and a force constant of ~40 N/m. Samples for top-down TEM analysis were prepared by floating the films off the PEDOT:PSS coated substrates and collecting on TEM grids with thin carbon films. Cross-sectional samples were prepared from the active area of the solar cell devices with a focused ion beam following our previously reported procedure.[44]

The top-down TEM images were processed prior to quantification by first applying a 2.3 nm Gaussian blur, followed by a fast Fourier transform bandpass filter with a 3−50 pixel range (pixel size 1.13 nm) and 5% tolerance of direction, and completed by thresholding to obtain a binary image. Following processing, the widths across approximately 150 individual domains were measured and an average width was calculated. Representative images displaying this process are included in the Supporting Information. All analysis was done in Image J.

Space-Charge-Limited Current (SCLC) Devices. Hole only SCLC devices were fabricated by cleaning the ITO as detailed above, and immediately following oxygen plasma exposure, the substrates were transferred into a thermal vapor deposition chamber. Approximately 5 nm of MoO_3 (Sigma Aldrich, 99.99% purity) was thermally evaporated with a chamber pressure of $2-4 \times 10^{-6}$ mbar. The prepared blend solutions were spin-cast as detailed previously, annealed, and transferred to the thermal evaporator where they remained under vacuum for 4−5 h prior to the thermal vapor deposition of 50 nm Au. The SCLC devices were of the same pixel configuration as that used for the OPV devices (8 pixels of 0.071 cm^2 area per substrate). The current−voltage characteristics were measured in the Ar atmosphere glovebox with a Keithley 2400 sourcemeter. This data was then fit with the field dependent SCLC eq 1 using Igor Pro to determine the zero-field hole mobility, μ_h, and the field dependent term, γ.[45−47]

$$J = \frac{9}{8}\mu_h \varepsilon_r \varepsilon_0 \exp(0.891\gamma\sqrt{V/L})\frac{V^2}{L^3}$$

(1)

where the film thicknesses, L, were measured by AFM to be 75 nm. A value of 3 was assumed for the relative permittivity, ε_r, and V is the measured voltage corrected for a built-in voltage, where applicable. Reported μ_h values are averages of at least 6−8 pixels with the error listed as ±1 standard deviation.

RESULTS AND DISCUSSION

The success of tailor-made additives to predictably control crystal nucleation and growth, along with the promising results from recent solution processed molecular BHJ OPVs,[6−8] inspired us to apply tailor-made additives for morphology control in molecular BHJ OPVs. To this end, the oligomers shown in Figure 2 were selected to control the crystallization of
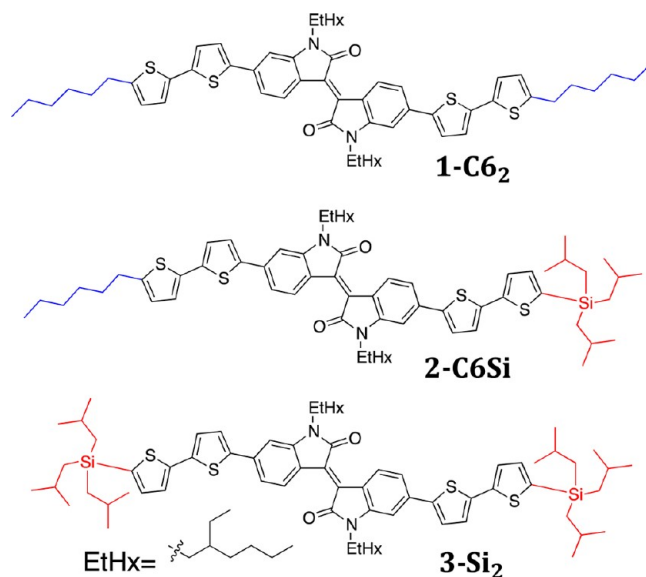

Figure 2. Molecular structure of the parent oligomer, **1-C6₂**, asymmetric additive, **2-C6Si**, and symmetric additive, **3-Si₂**.

1-C6₂.[43] Specifically, **2-C6Si** was designed such that one end of the oligomer contains the same end-group as the parent oligomer, i.e., a linear hexyl chain (**C6**), while the other end of the oligomer contains a bulky triisobutylsilyl group, denoted **Si** in the molecule's acronym. It was hypothesized that the **Si** end group would not be incorporated into the growing **1-C6₂** crystal due to its steric bulkiness; however, with the rest of the molecule being identical to the **1-C6₂** derivative, it would readily adsorb onto the growing **1-C6₂** crystals and thereby act to reduce the rate of **1-C6₂** crystal growth as illustrated in Figure 1. Consequently, as the ratio of **2-C6Si** to **1-C6₂** is increased, the **1-C6₂** crystallite sizes should be reduced, thus providing a facile method for fine tuning domain sizes in blend films for BHJ OPVs. The symmetric **3-Si₂** derivative was designed as a control material to determine if a symmetric additive can have a similar impact on film morphology and BHJ OPV device performance as the asymmetric analogue.

The high yield synthesis of **1-C6₂** was described in our first report of isoindigo-based conjugated small molecules.[43] Compared to the symmetric **1-C6₂**, the synthesis of the asymmetric **2-C6Si** would be possible in a step-by-step procedure, particularly involving the intermediate isolation of the asymmetric monobrominated precursor to the full molecule. However, to alleviate concerns over the synthetic cost of the tailor-made additive approach to active layer morphology control, we opted for a more convenient one-pot synthetic procedure affording both the main symmetric component (**1-C6₂**) and the asymmetric tailor-made additive (**2-C6Si**). This one-pot synthesis was carried out by the sequential addition of two different thienyl borolanes to a symmetric dibrominated isoindigo core under Suzuki cross-

Scheme 1. One-Pot Synthesis (a) of 1-C6$_2$ and 2-C6Si and Synthesis (b) of 3-Si$_2$[a]
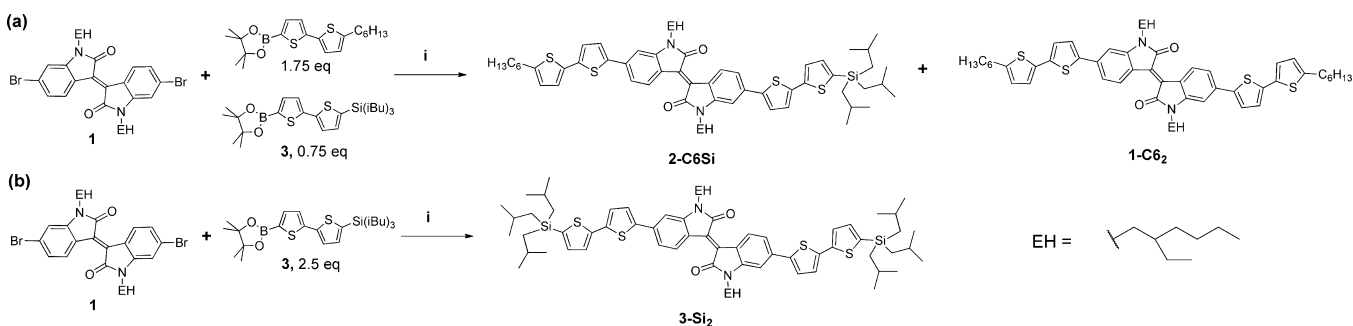
[a] (i) Pd$_2$(dba)$_3$, P(o-tyl)$_3$, Et$_4$NOH, toluene, 90 °C.
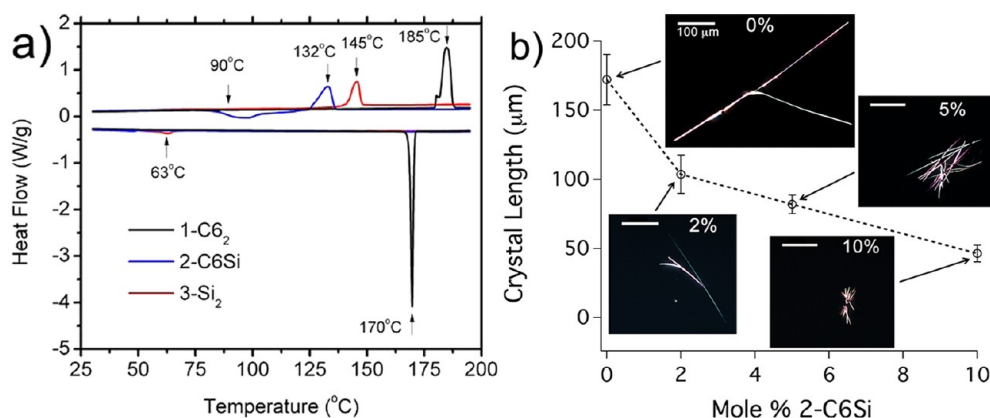

Figure 3. Differential scanning calorimetry (DSC) thermograms of **1-C6$_2$**, **2-C6Si**, and **3-Si$_2$** (a) and plot of crystal length vs mole percent of **2-C6Si** in solution with selected polarized light microscope images (b). All scale bars are 100 μm.

coupling conditions as shown in Scheme 1. The stoichiometry was chosen so that theoretically 65% of the starting material undergoing cross-coupling would afford **1-C6$_2$**, with the remaining 35% able to afford **2-C6Si**. Actual synthetic yields were 40% for **1-C6$_2$** and 29% for **2-C6Si**, resulting in an overall product yield of 69%. We anticipate that this one-pot procedure can likely be applied to other conjugated small molecules. The synthesis of the symmetric disilyl **3-Si$_2$** was performed separately, since the molecule was designed as a control compound.

The highest occupied molecular orbital (HOMO) levels of the three oligomers as probed through differential pulse voltammetry, Supporting Information Figure S1, are between −5.50 and −5.60 eV, while the lowest unoccupied molecular orbital (LUMO) levels of the oligomers are ca. −3.90 eV. Importantly for comparing the performance of the varying oligomers and oligomer blends in OPV cells and space-charge-limited current (SCLC) devices, the HOMO and LUMO levels of the three oligomers fall within a 0.08 and 0.03 eV range, respectively. These similar energy levels indicate that the materials should be able to be blended together without any of the materials acting as deep energetic traps.

Crystallization Behavior. Supporting our hypothesis that the asymmetric oligomer will act to inhibit crystallization, the differential scanning calorimetry (DSC) thermograms presented in Figure 3a display no crystallization peak for the asymmetric **2-C6Si** derivative, whereas a sharp crystallization peak is observed for **1-C6$_2$** at 170 °C. Furthermore, the DSC data displays an increase in melting points from 132 to 145 to 185 °C for **2-C6Si**, **3-Si$_2$**, and **1-C6$_2$** respectively. The lower

melting points and minimal to no crystallization peaks observed for the asymmetric **2-C6Si** and symmetric **3-Si$_2$** oligomers are attributed to the weaker intermolecular interactions afforded by the bulky triisobutylsilyl group(s). The lower melting point and lack of a crystallization peak for **2-C6Si** indicates that the asymmetric nature of the molecule further reduces intermolecular interactions and the ability for crystallization as compared to the addition of bulky groups alone (i.e., **3-Si$_2$**). This poor ability for crystallization is further supported by the reproducible observation of a broad exothermic peak (80−120 °C) prior to the melting peak, which is characteristic of a pre-melt crystallization. The presence of a pre-melt crystallization peak suggests that **2-C6Si** crystallizes too slowly for a peak to be observed during the cooling scan; thereby, a reorganization upon reheating is observed. Overall, these crystallization trends indicate the potential for **2-C6Si** and **3-Si$_2$** to be used as additives to decrease the crystallization rate of **1-C6$_2$**.

As may be expected from the different crystallization behavior observed through DSC, absorbance spectra of films of the neat materials show distinct features. In solution, the absorbance of all three oligomers is nearly identical with a λ_{max} of ca. 590 nm, yet in films, the spectral differences become evident as shown in Supporting Information Figure S2. As discussed in a prior manuscript,[48] the film of **1-C6$_2$** shows a dominant peak at ca. 600 nm and a prominent second peak at 655 nm that is indicative of intermolecular ordering/crystallinity. This 655 nm peak is absent for films of **2-C6Si** and **3-Si$_2$**, again indicating the repressed ability of these molecules to crystallize. Additionally, the aggregation behavior of **3-Si$_2$** differs significantly from **1-C6$_2$** and **2-C6Si**, as the main
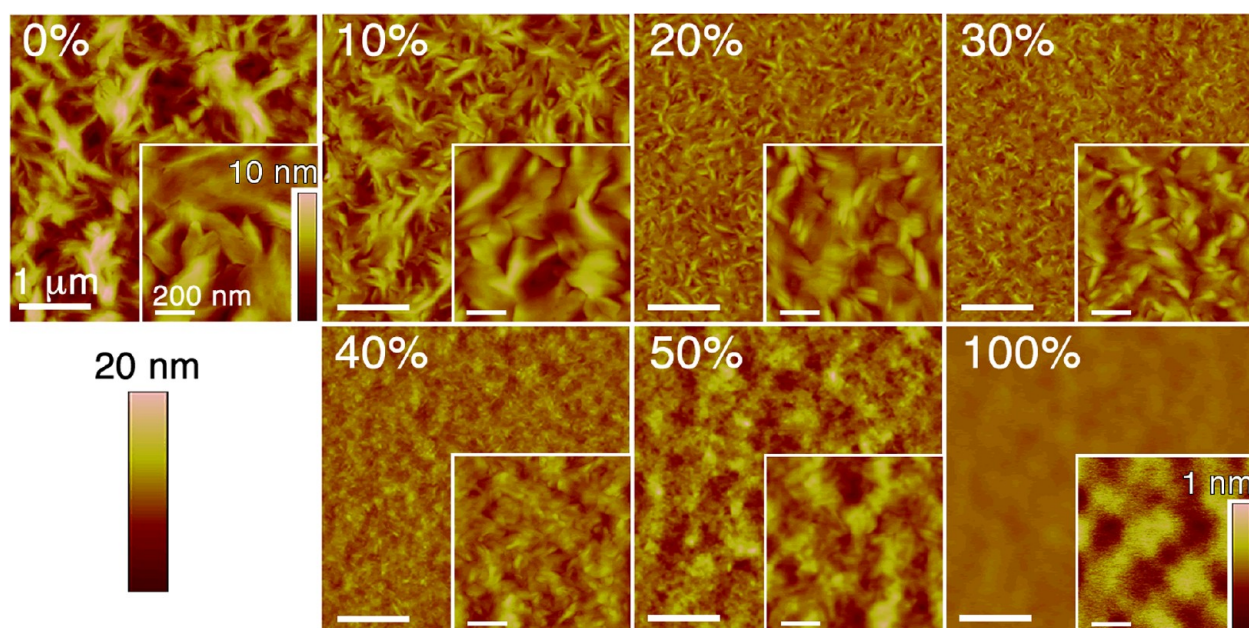
Figure 4. AFM height images of [**2-C6Si**:**1-C6₂**]:PC₆₁BM blend films, [**1**]:1 by weight, as the **2-C6Si** content is increased from 0 to 100%. All horizontal scale bars are 1 μm in large images and 200 nm in small inset images. Height scales are 20 nm (large images), 10 nm (insets 0−50%), and 1 nm (inset 100%).
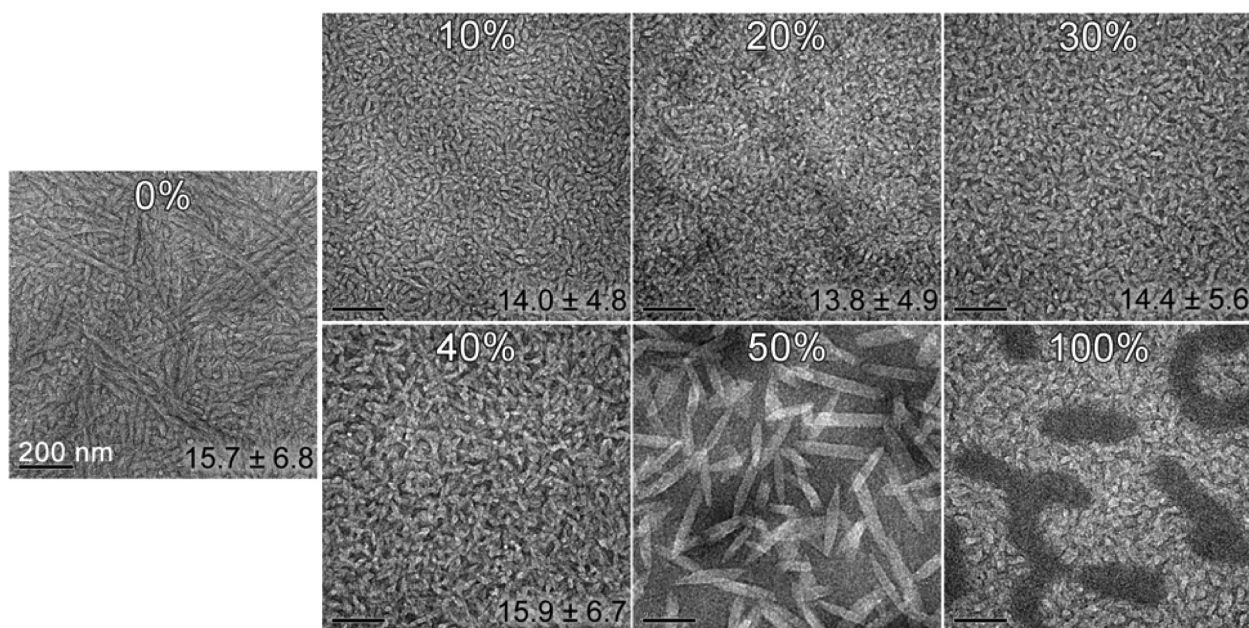

Figure 5. Bright-field TEM images of [**2-C6Si**:**1-C6₂**]:PC₆₁BM blend films, [**1**]:1 by weight, as the **2-C6Si** content is increased from 0 to 100%. The average domain widths in nanometers along with the standard deviations are provided in the bottom right corners of the images. All scale bars are 200 nm.

peak at ca. 590 nm in solution becomes only a small shoulder in film with a dominant peak appearing at 455 nm. These spectral differences reflect the difference in intermolecular packing between **1-C6₂** and **3-Si₂**, with **3-Si₂** displaying H-aggregation as opposed to J-aggregation for **1-C6₂**.

Solution crystallization experiments, the results of which are presented in Figure 3b, show that an increase in the relative concentration of **2-C6Si** to **1-C6₂** results in a decrease in crystal size. In these experiments, 0.05 mg/mL solutions of **1-C6₂** and **2-C6Si** in hexanes were prepared, with the relative concentration of **2-C6Si** to total solids varying from 0 to 100 mol %.

The hexane solutions were heated to 60 °C to completely dissolve the oligomers and allowed to cool to room temperature (22−25 °C) over 3 h, at which temperature the presence of crystals was observed. Subsequently, 10 μL of the solutions was deposited on clean glass or mica substrates for analysis with a polarized optical microscope or an atomic force microscope (AFM), respectively. Figure 3b shows that as the content of **2-C6Si** is increased from 0% to 10% the average crystal length decreases from 172 ± 10 to 46 ± 6 μm, with selected polarized optical microscope images displayed along with the measured averages. Note that error bars are given as ±
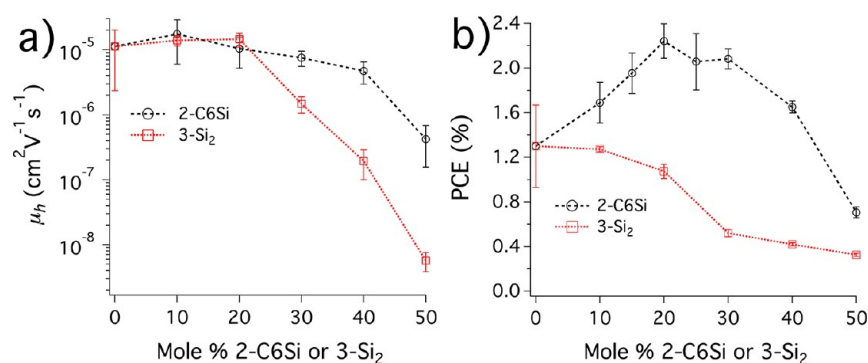
Figure 6. SCLC measured hole mobilities (a) and measured PCE under 100 mW/cm^2 AM1.5G illumination (b) for [2-C6Si:1-C6$_2$]:PC$_{61}$BM and [3-Si$_2$:1-C6$_2$]:PC$_{61}$BM devices, [1]:1 by weight, after 100 °C thermal annealing for 20 min.

Table 1. Performance Parameters of [2-C6Si:1-C6$_2$]:PC$_{61}$BM Blend OPV Cells under 100 mW/cm^2 Simulated AM1.5G Irradiation and Hole Mobilities Measured in the Dark for the Corresponding Films

2-C6Si content (%)	J_{SC} (mA/cm^2)	V_{OC} (V)	FF	PCE (%)	μ_h (×10^{-5} cm^{2}V^{-1}s^{-1})
0	4.58 ± 1.11	0.72 ± 0.04	0.39 ± 0.04	1.30 ± 0.37	1.1 ± 0.9
10	5.79 ± 0.27	0.75 ± 0.01	0.39 ± 0.02	1.69 ± 0.18	1.7 ± 1.1
15	5.86 ± 0.46	0.73 ± 0.01	0.45 ± 0.01	1.95 ± 0.18	
20	6.14 ± 0.27	0.82 ± 0.00	0.45 ± 0.02	2.24 ± 0.15	1.0 ± 0.5
25	5.66 ± 0.35	0.80 ± 0.01	0.45 ± 0.03	2.06 ± 0.25	
30	5.28 ± 0.17	0.81 ± 0.01	0.49 ± 0.02	2.08 ± 0.09	0.8 ± 0.2
40	4.54 ± 0.13	0.75 ± 0.01	0.49 ± 0.01	1.66 ± 0.05	0.5 ± 0.2
50	2.55 ± 0.12	0.69 ± 0.01	0.40 ± 0.01	0.71 ± 0.05	0.04 ± 0.03
100	1.17 ± 0.11	0.77 ± 0.05	0.24 ± 0.01	0.22 ± 0.04	0.002 ± 0.000

the standard error. Solutions were also prepared in the concentration range between 10 and 100%, with no crystal formation observed at these higher 2-C6Si concentrations. AFM images taken over the concentration range show the same crystalline features as observed with the polarized optical microscope, with no smaller crystallites apparent. Along with the DSC results, this solution crystallization data confirms our hypothesis that 2-C6Si can be used as an additive to control the size of 1-C6$_2$ crystals.

Film Morphologies. With the intended application of ultimately controlling domain sizes in BHJ OPVs, [2-C6Si:1-C6$_2$]:PC$_{61}$BM blend films, [1]:1 by weight, were cast onto PEDOT:PSS coated substrates and thermally annealed at 100 °C for 20 min to increase intermolecular ordering. In these films, the weight ratio of donor:PC$_{61}$BM was constant at [1]:1, while the mole percent of 2-C6Si relative to total donor concentration, i.e., 2-C6Si/(1-C6$_2$ + 2-C6Si) × 100, was increased from 0 to 100. As predicted, AFM height images of the blend films in Figure 4 show a decrease in feature size as the relative percent of 2-C6Si is increased from 0 to 40. As the composition is further increased to 50%, the surface roughness increases, followed by transitioning to a smooth and nearly featureless morphology at a 2-C6Si composition of 100%. The near featureless surface morphology at 100% 2-C6Si may be attributed to vertical phase separation with accumulation of 2-C6Si at the film surface, as will be further discussed later in the manuscript. The consistent decrease in feature size between 0 and 40% 2-C6Si indicates that the asymmetric oligomer can indeed function as an additive to provide fine scale control over film morphology. As discussed earlier and shown by the crystallization experiments, this decrease in domain size is attributed to the decrease in 1-C6$_2$ crystallite growth afforded by the structurally similar 2-C6Si derivative.

Consistent with the AFM images, bright-field transmission electron microscopy (TEM) images, as presented in Figure 5, show a decrease in both average domain width and domain width variation as the percentage of 2-C6Si increases from 0 to 20%. For the 0% blend film, the average domain width is 15.7 nm with a standard deviation of 6.8 nm, whereas for the 20% blend film, the average domain width is smaller at 13.8 nm and the domain widths are more uniform with a standard deviation of 4.9 nm. These domain sizes are on the high end of the typically reported 5−15 nm exciton diffusion lengths,[10−12] thereby even small increases in domain width will decrease the fraction of excitons that reach a D-A interface and dissociate. Furthermore, the larger standard deviation in domain size for the 0% film indicates that there are more large donor or acceptor rich domains in which the exciton will likely not be able to diffuse to a D-A interface. As demonstrated in a previous publication,[48] darker areas in the TEM images are fullerene rich domains whereas the lighter regions are oligomer rich.

In contrast to the AFM images though, small increases in domain sizes from 30 to 40%, 14.4 ± 5.6 to 15.9 ± 6.7 nm, respectively, and large increases from 50 to 100% 2-C6Si are observed. Interestingly, the large domains observed through TEM for the 50 and 100% films are not evident in the AFM images. Cross-sectional TEM images of the 100% film, Supporting Information Figure S3, indicate that these features are localized at the PEDOT:PSS interface; hence, they are not apparent in the AFM images of the film surface. Cross-sectional TEM images of the 20% 2-C6Si film also show signs of a vertical phase separated morphology, with an oligomer rich band bordering the top cathode followed immediately by a PC$_{61}$BM rich band. Below the PC$_{61}$BM rich band, the bulk of the 20% sample shows domains on the order of 10−30 nm. These domains are overall smaller and more uniform in size than the 0% 2-C6Si film.[48] The discrepancy between the

surface morphology as imaged by AFM and the bulk morphology as imaged by TEM has previously been observed for **1-C6$_2$**:PC$_{61}$BM blends and may be attributed to the top surface consisting of 90 ± 10 mol % **1-C6$_2$**, whereas the overall blend composition is 49 mol % **1-C6$_2$**.[48] This vertical phase separation with accumulation of the donor material at the top interface is in agreement with what has previously been observed for P3HT:PC$_{61}$BM blends.[49,50]

Mobility and Photovoltaic Performance. To determine the effect of the addition of **2-C6Si** on the mobilities in **1-C6$_2$**:PC$_{61}$BM blends, SCLC devices were constructed with [**2-C6Si:1-C6$_2$**]:PC$_{61}$BM blends and the hole mobilities (μ_h) were measured as detailed in the Supporting Information. As shown in Figure 6a and Table 1, as the percentage of **2-C6Si** is increased from 0 to 20%, the hole mobility remains nearly constant between 1.0×10^{-5} and 1.6×10^{-5} cm^{2}V^{-1}s^{-1}. The hole mobility begins to decrease as the concentration of **2-C6Si** is further increased, with an order of magnitude decrease between 40 and 50% **2-C6Si** and another order of magnitude decrease between the 50 and 100% devices. This trend would be consistent with a morphological model, where at low concentrations the **2-C6Si** molecules do not significantly affect the crystallinity within the **1-C6$_2$** domains; however, at higher concentrations, the **2-C6Si** molecules likely begin to inhibit the formation of ordered **1-C6$_2$** domains, and thus, a significant decrease in mobility occurs.

Photovoltaic devices consisting of [**1-C6$_2$:2-C6Si**]:PC$_{61}$BM blends, [1]:1 by weight, were fabricated on PEDOT:PSS coated ITO substrates and annealed at 100 °C for 20 min. Figure 6b and Table 1, along with the current density vs voltage curves in the Supporting Information, show that, as the relative composition of **2-C6Si** to total donor material is increased from 0 to 20%, a consistent increase in PCE occurs from 1.30 ± 0.37 to 2.24 ± 0.15%. This increase in PCE originates from a 34% increase in short circuit current (J_{SC}), a 14% increase in open circuit voltage (V_{OC}), and a 15% increase in fill factor (FF). The increase in J_{SC} corresponds well with the decreased domain sizes as imaged through AFM and TEM; i.e., the result of these smaller domains is that more excitons are created within an exciton diffusion length of a D-A interface. In fact, the trend in J_{SC} is identical to the trend in the measured domain widths throughout the entire **2-C6Si** concentration range, with these measured widths displayed in the TEM images shown in Figure 5. Although the increases in V_{OC} and FF are uncertain, they may potentially both be attributed to decreased recombination and/or shifts in energy of the charge-transfer state formed between oligomer and fullerene resulting from the bulky triisobutylsilyl end group.[51] Importantly, the statistical variation in device performance decreases upon addition of **2-C6Si**, as indicated by the error bars that are given as ±1 standard deviation. The PCE is fairly constant between 20% and 30% **2-C6Si**, after which point it begins to decrease. At 50 and 100% **2-C6Si**, the PCE has decreased to 0.71% and 0.22%, respectively. The decreased PCE at high concentrations is attributed to the lower hole mobilities as well as the large scale phase separation as evidenced in the TEM images.

Symmetric 3-Si$_2$ Derivative. The morphology, mobility, and OPV device performance studies were performed in an identical way for **3-Si$_2$** as was done for **2-C6Si** to provide insight as to the effect of the symmetry of the molecule. The AFM images, as shown in Supporting Information Figure S7, for [**3-Si$_2$:1-C6$_2$**]:PC$_{61}$BM blends with **3-Si$_2$** compositions of 10 and 20% show a similar trend as was observed for **2-C6Si**. At

higher **3-Si$_2$** content, the morphology begins to differ from that of the [**2-C6Si:1-C6$_2$**]:PC$_{61}$BM blends, with large increases in surface roughness and feature size at **3-Si$_2$** concentrations of 50 and 100%. The TEM images presented in Figure S8 (Supporting Information) differ from those of the **2-C6Si:1-C6$_2$** blends at concentrations of 10 and 20%, with the [**3-Si$_2$:1-C6$_2$**]:PC$_{61}$BM blends displaying slightly smaller and less well-defined features. In agreement with the AFM images, at increased **3-Si$_2$** concentrations, large-scale phase separation is observed in the TEM images with large crystalline features appearing.

The SCLC measured hole mobilities presented in Figure 5a display a similar trend as those of the [**2-C6Si:1-C6$_2$**]:PC$_{61}$BM blends at low **3-Si$_2$** compositions; however, at 30% **3-Si$_2$** content, the mobility of the [**3-Si$_2$:1-C6$_2$**]:PC$_{61}$BM blend decreases sharply as it becomes 1 to 2 orders of magnitude lower than the [**2-C6Si:1-C6$_2$**]:PC$_{61}$BM blends. OPV devices based on [**3-Si$_2$:1-C6$_2$**]:PC$_{61}$BM blends show no increase in OPV performance as compared to the device with no **3-Si$_2$**. On the basis of the TEM images of the 10% and 20% blends, the absence of any performance increase may be attributed to a more intermixed morphology that would hinder charge extraction and increase charge recombination. Although we do not have a more definitive explanation for the decreased performance of the **3-Si$_2$** containing OPV cells relative to the **2-C6Si** containing cells, it is clear that the asymmetric oligomer induces an enhancement in PCE, making it a more beneficial additive than the symmetric triisobutylsilyl substituted derivative.

CONCLUSION

The use of tailor-made oligomers has been shown as an effective route to precisely control the size of crystalline domains and, thus, the morphology of oligomer/PC$_{61}$BM blend films with applications for OPVs. The asymmetric **2-C6Si** oligomer was shown to reduce the size of **1-C6$_2$** crystals in solution and controllably reduce domain sizes in [**2-C6Si:1-C6$_2$**]:PC$_{61}$BM blend films. The reduced domain sizes and relatively high hole mobilities in [**2-C6Si:1-C6$_2$**]:PC$_{61}$BM blend films at low **2-C6Si** concentrations led to improved OPV performance, with a PCE increase from 1.3 to 2.2% as the content of **2-C6Si** relative to total donor material was increased from 0 to 20%. Contrary to the asymmetric oligomer, addition of the symmetrically substituted **3-Si$_2$** oligomer did not result in improved OPV performance. These results indicate that the asymmetry of the tailor-made oligomer in this case is important for increased OPV performance. Overall, the study shows the potential of tailor-made additives to predictably control morphology in small molecule-based BHJ OPVs. With the high level of control on crystal size, shape, and growth rate afforded by tailor-made additives, it can easily be foreseen how these may play a major role in controlling film morphologies in organic electronic devices such as OFETs and BHJ OPVs.

ASSOCIATED CONTENT

Ⓢ Supporting Information

Absorbance spectra, cyclic voltammograms, space-charge limited current data, and current−voltage characteristics for the OPV devices. This material is available free of charge via the Internet at http://pubs.acs.org.

■ AUTHOR INFORMATION

Corresponding Author

*E-mail: Grahamk@stanford.edu (K.R.G.); Reynolds@chemistry.gatech.edu (J.R.R.).

Author Contributions

The manuscript was written through contributions of all authors. All authors have given approval to the final version of the manuscript.

Notes

The authors declare no competing financial interest.

■ REFERENCES

(1) Chen, H.-Y.; Hou, J.; Zhang, S.; Liang, Y.; Yang, G.; Yang, Y.; Yu, L.; Wu, Y.; Li, G. *Nat. Photonics* **2009**, *3*, 649−653.

(2) Zhou, H.; Yang, L.; Stuart, A. C.; Price, S. C.; Liu, S.; You, W. *Angew. Chem., Int. Ed.* **2011**, *50*, 2995−2998.

(3) He, Z.; Zhong, C.; Huang, X.; Wong, W.-Y.; Wu, H.; Chen, L.; Su, S.; Cao, Y. *Adv. Mater.* **2011**, *23*, 4636−4643.

(4) Small, C. E.; Chen, S.; Subbiah, J.; Amb, C. M.; Tsang, S.-W.; Lai, T.-H.; Reynolds, J. R.; So, F. *Nat. Photonics* **2011**, *6*, 115−120.

(5) Li, Z.; He, G.; Wan, X.; Liu, Y.; Zhou, J.; Long, G.; Zuo, Y.; Zhang, M.; Chen, Y. *Adv. Energy Mater.* **2011**, *2*, 74−77.

(6) Sun, Y.; Welch, G. C.; Leong, W. L.; Takacs, C. J.; Bazan, G. C.; Heeger, A. J. *Nat. Mater.* **2012**, *11*, 44−48.

(7) Walker, B.; Tomayo, A. B.; Dang, X. D.; Zalar, P.; Seo, J. H.; Garcia, A.; Tantiwiwat, M.; Nguyen, T. Q. *Adv. Funct. Mater.* **2009**, *19*, 3063−3069.

(8) Loser, S.; Bruns, C. J.; Miyauchi, H.; Ortiz, R. P.; Facchetti, A.; Stupp, S. I.; Marks, T. J. *J. Am. Chem. Soc.* **2011**, *133*, 8142−8145.

(9) Shang, H.; Fan, H.; Liu, Y.; Hu, W.; Li, Y.; Zhan, X. *Adv. Mater.* **2011**, *23*, 1554−1557.

(10) Scully, S. R.; McGehee, M. D. *J. Appl. Phys.* **2006**, *100*, 34907.

(11) Lunt, R. R.; Giebink, N. C.; Belak, A. A.; Benziger, J. B.; Forrest, S. R. *J. Appl. Phys.* **2009**, *105*, 053711.

(12) Shaw, P. E.; Ruseckas, A.; Samuel, I. D. W. *Adv. Mater.* **2008**, *20*, 3516−3520.

(13) Ma, W.; Heeger, A. J. *Adv. Funct. Mater.* **2005**, *15*, 1617−1622.

(14) Savenije, T. J.; Loos, J. *Adv. Funct. Mater.* **2005**, *15*, 1260−1266.

(15) Li, G.; Yao, Y.; Yang, H.; Shrotriya, V.; Yang, G.; Yang, Y. *Adv. Funct. Mater.* **2007**, *17*, 1636−1644.

(16) Miller, S.; Fanchini, G.; Lin, Y. Y.; Li, C.; Chen, C. W.; Su, W. F.; Chhowalla, M. *J. Mater. Chem.* **2008**, *18*, 306−312.

(17) Peet, J.; Kim, J. Y.; Coates, N. E.; Ma, W. L.; Moses, D.; Heeger, A. J.; Bazan, G. C. *Nat. Mater.* **2007**, *6*, 497−500.

(18) Corey, V. H.; Xuan-Dung, D.; Robert, C. C.; Jeff, P.; Thuc-Quyen, N.; Guillermo, C. B. *Adv. Mater.* **2010**, *22*, E63−E66.

(19) Walker, B.; Tamayo, A.; Duong, D. T.; Dang, X.-D.; Kim, C.; Granstrom, J.; Nguyen, T.-Q. *Adv. Energy Mater.* **2011**, *1*, 221−229.

(20) Winzenberg, K. N.; Kemppinen, P.; Fanchini, G.; Bown, M.; Collis, G. E.; Forsyth, C. M.; Hegedus, K.; Singh, T. B.; Watkins, S. E. *Chem. Mater.* **2009**, *21*, 5701−5703.

(21) Krebs, F. C.; Gevorgyan, S. A.; Alstrup, J. *J. Mater. Chem.* **2009**, *19*, 5442−5451.

(22) Shaheen, S. E.; Radspinner, R.; Peyghambarian, N.; Jabbour, G. E. *Appl. Phys. Lett.* **2001**, *79*, 2996.

(23) Hoth, C. N.; Schilinsky, P.; Choulis, S. A.; Brabec, C. J. *Nano Lett.* **2008**, *8*, 2806−2813.

(24) Roncali, J. *Adv. Energy Mater.* **2011**, *1*, 147−160.

(25) Darling, S. B. *Energy Environ. Sci.* **2009**, *2*, 1266−1273.

(26) Miyanishi, S.; Zhang, Y.; Tajima, K.; Hashimoto, K. *Chem. Commun.* **2010**, *46*, 6723−6725.

(27) Zhang, F.; Svensson, M.; Andersson, M. R.; Maggini, M.; Bucella, S.; Menna, E.; Inganäs, O. *Adv. Mater.* **2001**, *13*, 1871−1874.

(28) Sivula, K.; Ball, Z. T.; Watanabe, N.; Fréchet, J. M. J. *Adv. Mater.* **2006**, *18*, 206−210.

(29) Sary, N.; Richard, F.; Brochon, C.; Leclerc, N.; Lévêque, P.; Audinot, J.-N.; Berson, S.; Heiser, T.; Hadziioannou, G.; Mezzenga, R. *Adv. Mater.* **2010**, *22*, 763−768.

(30) Lee, J. U.; Jung, J. W.; Emrick, T.; Russell, T. P.; Jo, W. H. *J. Mater. Chem.* **2010**, *20*, 3287−3294.

(31) Eckert, J.-F.; Nicoud, J.-F.; Nierengarten, J.-F.; Liu, S.-G.; Echegoyen, L.; Barigelletti, F.; Armaroli, N.; Ouali, L.; Krasnikov, V.; Hadziioannou, G. *J. Am. Chem. Soc.* **2000**, *122*, 7467−7479.

(32) Bu, L.; Guo, X.; Yu, B.; Qu, Y.; Xie, Z.; Yan, D.; Geng, Y.; Wang, F. *J. Am. Chem. Soc.* **2009**, *131*, 13242−13243.

(33) Richards, J. J.; Rice, A. H.; Nelson, R. D.; Kim, F. S.; Jenekhe, S. A.; Luscombe, C. K.; Pozzo, D. C. *Adv. Funct. Mater.* **2012**, DOI: 10.1002/adfm.201201100.

(34) Addadi, L.; Berkovitch-Yellin, Z.; Weissbuch, I.; van Mil, J.; Shirnon, L. J. W.; Lahav, M.; Leiserowitz, L. *Angew. Chem., Int. Ed.* **1985**, *24*, 466−485.

(35) Berkovitch-Yellin, Z.; van Mil, J.; Addadi, L.; Idelson, M.; Lahav, M.; Leiserowitz, L. *J. Am. Chem. Soc.* **1985**, *107*, 3111−3122.

(36) Weissbuch, I.; Addadi, L.; Leiserowitz, L. *Science* **1991**, *253*, 637−645.

(37) Lechuga-Ballesteros, D.; Rodriguez-Hornedo, N. *J. Colloid Interface Sci.* **1993**, *157*, 147−153.

(38) Garnier, S.; Petit, S.; Coquerel, G. *J. Cryst. Growth* **2002**, *234*, 207−219.

(39) van Enckevort, W. J. P.; Los, J. H. *J. Phys. Chem. C* **2008**, *112*, 6380−6389.

(40) Oliveira, D.; Baba, K.; Mori, J.; Miyashita, Y.; Kasai, H.; Oikawa, H.; Nakanishi, H. *J. Cryst. Growth* **2010**, *312*, 431−436.

(41) Lee, B. S. S.; Kim, C. S.; Gomez, E. D.; Purushothaman, B.; Toney, M. F.; Wang, C.; Hexemer, A.; Anthony, J. E.; Loo, Y.-L. *Adv. Mater.* **2009**, *21*, 3605−3609.

(42) Fraboni, B.; Femoni, C.; Mencarelli, I.; Setti, L.; Di Pietro, R.; Cavallini, A.; Fraleoni-Morgera, A. *Adv. Mater.* **2009**, *21*, 1835−1839.

(43) Mei, J.; Graham, K. R.; Stalder, R.; Reynolds, J. R. *Org. Lett.* **2010**, *12*, 660−663.

(44) Amb, C. M.; Chen, S.; Graham, K. R.; Subbiah, J.; Small, C. E.; So, F.; Reynolds, J. R. *J. Am. Chem. Soc.* **2011**, *133*, 10062−10065.

(45) Bozano, L.; Carter, S. A.; Scott, J. C.; Malliaras, G. G.; Brock, P. J. *Appl. Phys. Lett.* **1999**, *74*, 1132−1134.

(46) Scott, J. C.; Brock, P. J.; Salem, J. R.; Ramos, S.; Malliaras, G. G.; Carter, S. A.; Bozano, L. *Synth. Met.* **2000**, *111-112*, 289−293.

(47) Bisquert, J.; Montero, J. M.; Bolink, H. J.; Barea, E. M.; Garcia-Belmonte, G. *Phys. Status Solidi A* **2006**, *203*, 3762−3767.

(48) Graham, K. R.; Stalder, R.; Wieruszewski, P.; Hartell, M.; Mei, J.; So, F.; Reynolds, J. R. *Adv. Funct. Mater.* **2012**, *22*, 4801−4813.

(49) Xu, Z.; Chen, L.-M.; Yang, G.; Huang, C.-H.; Hou, J.; Wu, Y.; Li, G.; Hsu, C.-S.; Yang, Y. *Adv. Funct. Mater.* **2009**, *19*, 1227−1234.

(50) Wang, H.; Gomez, E. D.; Kim, J.; Guan, Z.; Jaye, C.; Fischer, D. A.; Kahn, A.; Loo, Y.-L. *Chem. Mater.* **2011**, *23*, 2020−2023.

(51) Vandewal, K.; Tvingstedt, K.; Gadisa, A.; Inganäs, O.; Manca, J. V. *Phys. Rev. B* **2010**, *81*, 1−8.